

HRC-I Gain Correction

J. Posson-Brown, V. Kashyap

Mar 2007

Abstract

We study the gain variations in the HRC-I over the duration of the *Chandra* mission. We analyze calibration observations of AR Lac obtained yearly at the nominal aimpoint and at 20 offset locations on the detector. We show that the gain is declining, and that the time dependence of the gain can be modeled generally as a linear decrease in PHAs. We describe the spatial and temporal characteristics of the gain decline and discuss the creation of time-dependent gain correction maps. These maps are used to convert PHAs to PI channels, thereby removing spatial and temporal dependence, and allowing source pulse-height distributions to be compared directly regardless of observation date or location on the detector.

1 Introduction

Regular monitoring of both the HRC-I and the HRC-S have shown that there exists a steady decline of the gain since the launch of the *Chandra* observatory (Posson-Brown & Donnelly 2003, Pease & Drake 2003). The gain decline takes the form of a shift in the pulse height amplitude (PHA) profiles of observed sources to lower detector channels, and is expected to occur as the cumulative dosage on the MCPs increases (Juda 2001).

Gain monitoring serves as a proxy for the health of the HRC instruments. It is therefore necessary to establish a baseline behavior of the gain drop so that departures from it can be detected quickly. Here we describe the characteristics of the spatial and temporal gain corrections on the HRC-I, and develop tools that can also be applied to the HRC-S (Posson-Brown et al., memo in preparation).

Furthermore, the low background, large field-of-view, and the comparatively high oversampling of the *Chandra* PSF provided by the HRC-I makes it an attractive instrument for large area surveys. The main hindrance to this type of usage is the poor spectral resolution of the micro-channel plate detectors. However, while poor, the detectors are capable of sufficient spectral discrimination to allow crude estimates of the spectral shape via hardness ratios and quantile-width diagrams (Kashyap & Posson-Brown 2005). In order to facilitate such usage, it is necessary to calibrate the PHA values such that any spatial and temporal variations are accounted for.

1.1 Pre-Flight Gain Calibration

The HRC-I gain response was measured during pre-flight ground calibration with a series of flat field maps at different energies (see Table 1). Gain maps were created for each energy by calculating the median PHA value for the events over the detector in half-tap (128 x 128 pixels) bins. Each map was then normalized by the mean value in its central $\frac{1}{9}$ area, thus generating, in its reciprocal, a multiplicative gain correction map, designed to modify the off-axis PHAs to match the PHAs in the center of the detector and thus create “pulse invariant” (PI) pulse height units. Finally, these

normalized correction maps were averaged to create a single “pre-flight gain map” for the detector (Wilton et al. 2005). This gain correction map is available in the *Chandra* Calibration Database as the file

`$CALDB/data/chandra/hrc/bcf/gain/hrcid1998-10-30gainN0002.fits`

Table 1: Pre-flight energy to PHA gain mapping

Source	Energy [eV]	Mean Central PHA
B $K\alpha$	183	97.55
C $K\alpha$	277	98.06
O $K\alpha$	525	127.24
Al $K\alpha$	1487	151.36
Ti $K\alpha$	4511	157.30
Fe $K\alpha$	6404	174.61

On October 4, 1999, shortly after launch, the voltage on the HRC-I MCP was lowered. A series of calibration observations of AR Lac were carried out at the aimpoint and 20 offset locations at both the high and the new flight voltage settings to determine any changes to the gain.

We computed a new gain correction map for the flight voltage settings based on these observations (see Wilton et al. 2005), following a process which will be discussed in §5.1. This map is available in the *Chandra* CALDB as the gain correction map for flight voltage observations:¹

`$CALDB/data/chandra/hrc/bcf/gain/hrcid1999-10-04gainN0003.fits`

Here, we derive gain correction maps at the flight voltage that correct for both spatial and temporal variations in the gain. We describe the observations used to derive the new gain correction maps in §2, and the data reduction steps in §3. Characteristics of the PHA temporal decline are discussed in §4, and the time dependent gain maps are computed in §5. Finally, we discuss our analysis in §6 and summarize our results in §7.

2 Observations

In order to monitor the gain response of the HRC-I, yearly calibration observations are taken of AR Lac (Table 2) at 21 locations on the detector (see Figure 1). The observations in each yearly set are done successively, or, if this is not possible (due to an interruption such as a radiation shut-down), they are done as closely together as possible. Each observation is nominally 1 ks long; however, effective observation times may be shorter because of background flares (see Table 3).

After the operating voltage of the HRC-I was lowered on 4 October 1999 (see §1.1), we have obtained 8 sets of AR Lac observations at the current (low) voltage. These observations were carried out in October 1999 (AO 1), December 1999 (AO 1), December 2000 (AO 2), January 2002 (AO 3), February 2003 (AO 4), November 2004 (AO 5), October 2005 (AO 6), and September 2006 (AO 7). The ObsIDs for all observations used in the analysis presented here are listed in Table 3, along with the deadtime and effective (post-filtering) exposure time.

¹Note that the date encoded in the filename, 4 October 1999, marks the beginning of the calibration program to obtain data at different voltage settings. Therefore, for any observations carried out at the high voltage setting after this date, the `gainfile` parameter in `hrc_process_events` must be manually and explicitly set to use the pre-flight gain correction map.

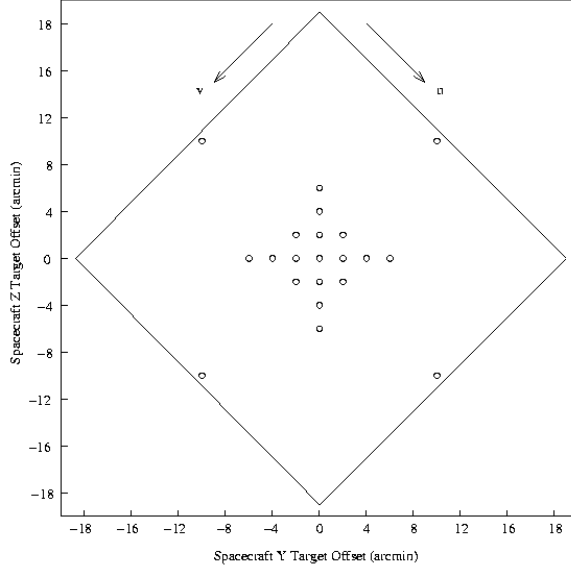


Figure 1: Locations of AR Lac observations on the HRC-I. Calibration observations are carried out at the aimpoint and 20 offset locations each cycle in order to monitor the gain: $(Y_{\text{sim}}, Z_{\text{sim}}) = (0', 0'), (0', \pm 2'), (\pm 2', 0'), (\pm 2', \pm 2'), (0', \pm 4'), (\pm 4', 0'), (0', \pm 6'), (\pm 6', 0'),$ and $(\pm 10', \pm 10')$

Table 2: AR Lac stellar parameters

Parameter	Value
Other Names	HR 8448 / HD 210334 / RX J2208.6+4544 / HIP 109303
$(\text{RA,Dec})_{\text{ICRS2000.0}}$	(22:08:40.818, +45:44:32.12)
$m_V, B-V$	6.13, 0.72
Distance	42–47 pc
Spectral Type	G2IV/K0IV (RS CVn)
M_V	3.5/3.3
Masses	1.3/1.3 M_{\odot}
Radii	1.8/3.1 R_{\odot}
Ephemeris	1.98316 ^d ; conjunction @ 2445611.6290 HJD

3 Data Reduction

A pulse height amplitude (PHA) is assigned to each event based on the total charge collected by the cross-grid charge detector (CGCD) of the HRC-I and is recorded in the Level 1 event lists. We monitor the gain response by tracking the median PHA over time at each of the 21 observation locations. In all cases, we first reduce the data with CIAO (v3.4; CALDB v3.3) and analyze the data with pre-packaged and custom-built IDL routines (e.g., PINTofALE; Kashyap & Drake 2000). The detailed processing sequence for each ObsID is laid out below:

1. Make new Level 1 event lists by
 - first checking the `rangelev` and `widthres` keywords in the header of the `evt1` file, and add them if necessary;
 - making a new bad pixel file with the current version of the `degap` file; and

- running `hrc_process_events` with the current CALDB products (and the newly computed bad pixel file), and setting the parameter `gainfile=NONE` to make a new `evt1` file.
- 2. Make a detector-wide lightcurve binned at 10 s from the newly computed `evt1` file, thus incorporating the default good time intervals (GTIs) for the ObsID.²
- 3. Create new GTI filters by excluding those times when the lightcurve exceeds 150 ct s^{-1} (safely under the telemetry saturation limit of 184 ct s^{-1}).
- 4. Filter the events on these new GTIs to obtain a new Level 1 event list.
- 5. Update the deadtime corrections for the new GTIs by using `hrc_dtfstats` to make a new DTF file, then updating the `DTCOR` and `EXPOSURE` keywords in the header of the new GTI filtered `evt1` file.

We extract source events from an 800x800 box centered on the nominal observation location in chip coordinates. Background is estimated by collecting the events in the *same location*, but from the 20 other observations carried out in that cycle. The background counts thus accumulated are normalized by their appropriate exposure times prior to subtracting them from the counts accumulated at the source location. The median values of the source PHA spectrum are estimated using Monte Carlo simulations.³

Observations carried out during AO6 were heavily contaminated by excessive background and 10 of them were completely telemetry saturated. We verified that the source PHA spectrum is not significantly altered by the telemetry saturation (the background-subtracted PHA spectra from times of telemetry saturation are statistically indistinguishable from those at low background, for data obtained during the same ObsID),⁴ and did not carry out the additional GTI filtering for those datasets which are completely telemetry saturated. Background for these datasets were obtained from similarly saturated datasets. That is, we calculated the background for telemetry saturated observations from the other telemetry saturated observations, and we did not use the telemetry saturated observations when calculating the background for unaffected observations.

Note that we use Level 1 event lists for this analysis. The median PHAs derived from Level 2 events are systematically lower than those derived from Level 1 events, but only by ~ 1 channel on average. Moreover, the average best-fit scale factor for matching the Level 2 to Level 1 aimpoint PHA spectra is 1.00 ± 0.01 . The lack of difference is not surprising, because AR Lac is a strong source ($\sim 5 \text{ ct s}^{-1}$); because we actively remove background, in addition to filtering out intervals of strong background, the spectral features are dominated by the source. Thus, we conclude that, as long as the background-subtraction is done carefully, it makes no difference whether we use Level 1 or Level 2 event lists for our analysis. We choose to use the former, as the gain maps will be applied to Level 1 event lists in pipeline processing. Furthermore, using Level 1 events has the advantage

²For the Oct 99 observations done in conjunction with the HRC-I voltage adjustment, we use a set of GTIs based on when the voltage was stable at the low setting (Juda, private communication) in place of the default GTIs.

³For each detector channel, the posterior probability distribution of the source intensity is computed, taking into account the measured background (van Dyk et al. 2001). Source counts realizations are repeatedly drawn from this distribution and the median is computed at each iteration. The average value of the medians obtained from such Monte Carlo simulations is reported as the median PHA and the standard deviation of the sample as the 1σ errors on it.

⁴We grouped the ObsIDs into those that were completely telemetry-saturated ($> 90\%$; 10 ObsIDs) and those that were partially telemetry saturated ($< 50\%$; 11 ObsIDs). The aimpoint observation (ObsID 5979) is telemetry saturated $\approx 40\%$ of the time. We filter this observation into the two parts, construct PHA spectra, and compute the best-fit scale factor that, when multiplying the telemetry saturated PHA values, matches the non-telemetry-saturated PHA spectra. We find that this scale factor is 1.03 ± 0.01 , which means that the two are practically indistinguishable, and that telemetry saturation has no measurable effect on the background-subtracted spectra.

that it is less affected by changes to pipeline processing and results in a more stable calibration product.

4 Characteristics of PHA Decline

The median PHAs, calculated as described in §3, are shown in Figure 2 as a function of observation location. The gain response decreases steadily and monotonically at all the monitored locations, as evidenced by the consistent lowering of the median PHAs. (But note the large drop in median PHA at the aimpoint between December 1999 and December 2000.) The errors on the medians are typically ≤ 1 channel.

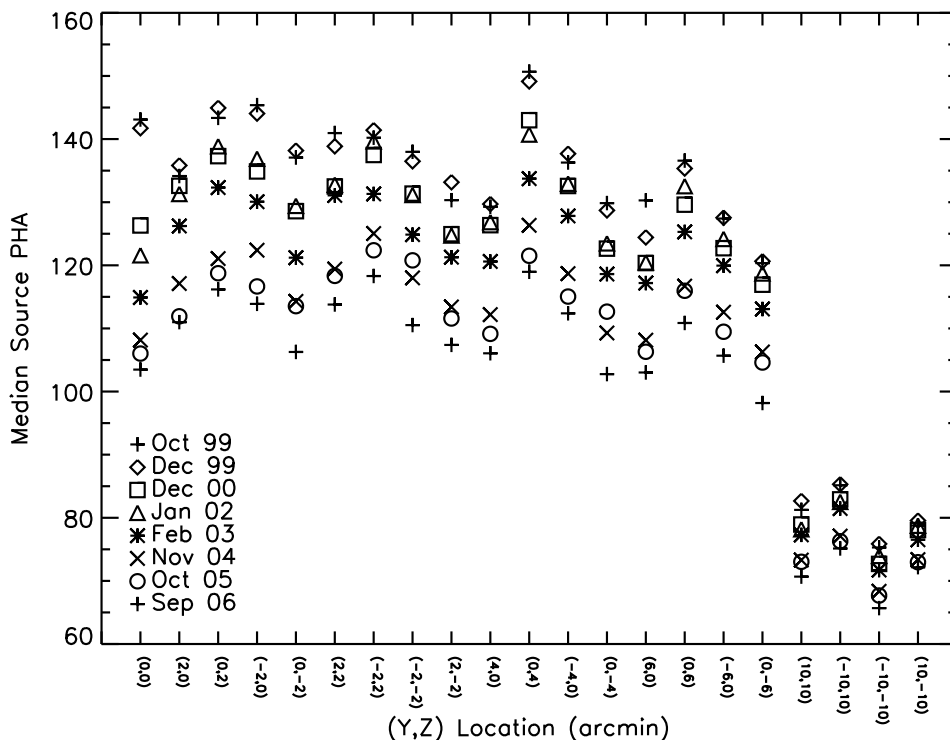


Figure 2: Median PHAs for HRC-I AR Lac observations. The background subtracted median PHAs are plotted in a vertical row for all observations at a given location, for data obtained during different cycles, all at the low voltage setting. Data from different cycles are marked with different point types (see legend). The statistical errors on the medians are typically ≤ 1 channel. Note that the median PHAs drop monotonically.

With the exception of the aimpoint, the time dependent decrease in the median PHAs at all the locations are all well-fit by straight lines (see Figure 3). Even the data from the aimpoint can be well-fit by a straight line after December 2000. It is apparent that the aimpoint underwent an as yet unexplained stressing that resulted in a large gain drop soon after the voltage was lowered. With that exception, the gain drop is well-fit as a linear decrease at all locations and at all times. Furthermore, the best-fit slopes are roughly equal for all cases (excluding the four pointings at 14.14' off-axis), indicating that the rate of gain decline is relatively uniform across the detector (Figure 4).

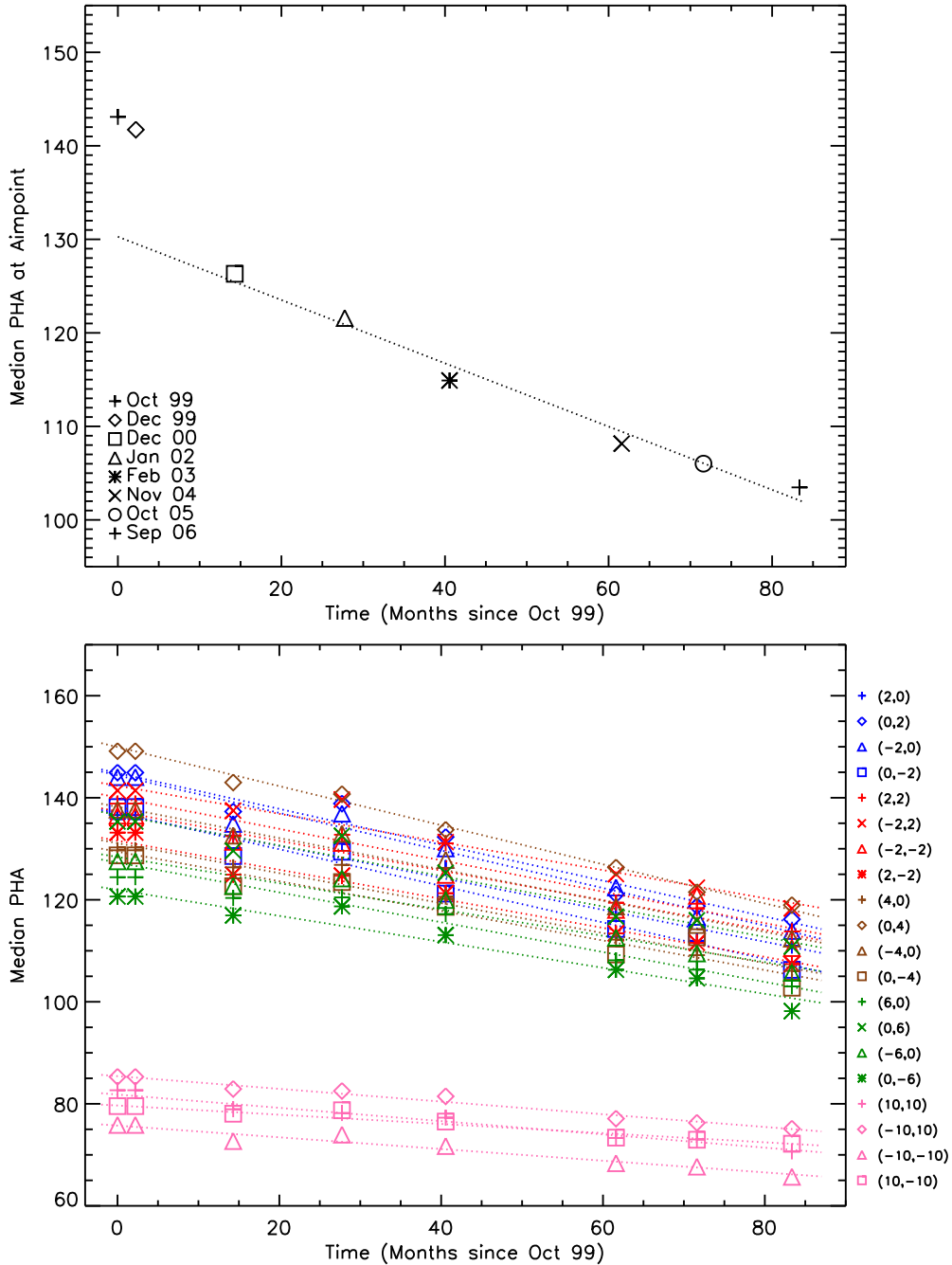


Figure 3: Linear fits to the median PHAs at different locations. The errors on the medians are ≤ 1 channel. **Top:** Median PHAs at the airpoint of the HRC-I as a function of time. The median PHAs from different times are marked with different symbols (see legend). The straight line fit is carried out excluding the Oct and Dec 99 data. Note the large drop in gain between Dec 99 and Dec 00. **Bottom:** Median PHAs at all offset locations as a function of time. Data from different locations are marked with different symbols (see legend), and are fit with straight lines.

4.1 Curvature Test

There are many factors that cause the dosage to vary with time, which in turn will affect the gain. These include both astrophysical causes such as the solar cycle, which is anti-correlated with the

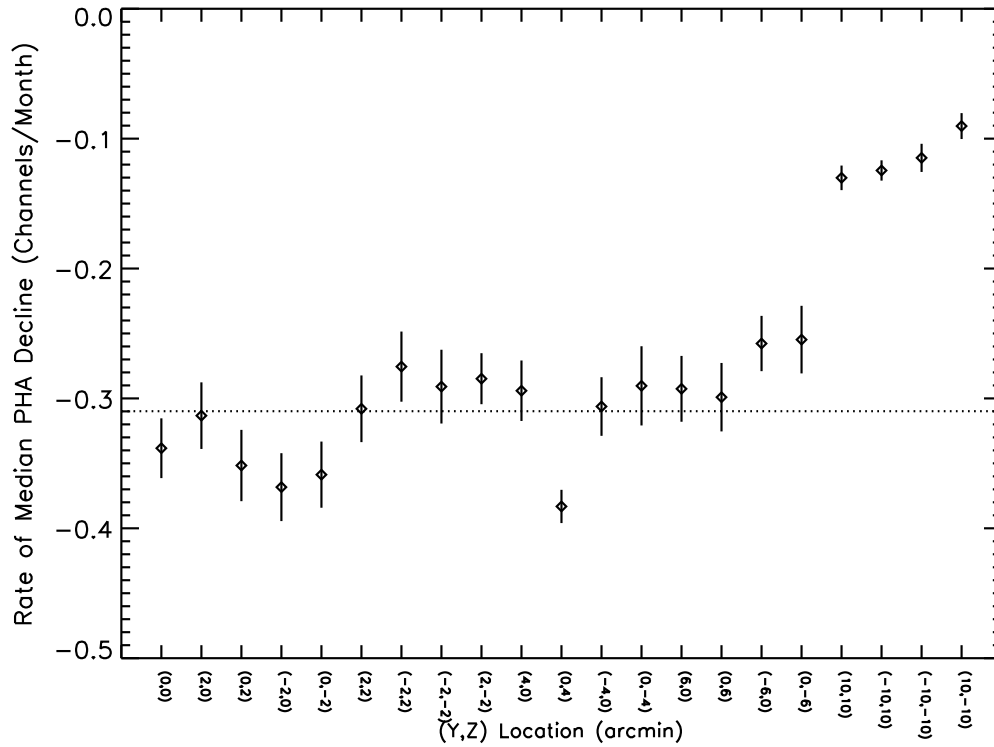


Figure 4: Uniformity of gain decline across the HRC-I. The best-fit slopes from the linear fits to the median PHAs (Figure 3) are shown for each location. The average of the slopes (neglecting the four pointings at 14.14' offaxis) is shown as the dotted horizontal line. To a first approximation, excluding the far offaxis locations, the gain decline is uniform across the detector.

proton flux on the detector, and instrumental causes such as changes in the flight settings. For instance, on October 12, 2003, the Chandra flight settings were changed to keep the HRC door open at all times. Previously, it was closed during radiation zone passages and safing events to protect the detector. However, after a motor select relay for one of the shutters failed, preventing the shutter from being inserted, there was concern that, if the similar relay used in operation of the door failed when the door was shut, the HRC could become unusable (Juda 2004). Coincidentally, this was also the time that the solar cycle was descending into a minimum.⁵ Thus, even though the drop in median PHAs can be well-fit by straight lines (Figure 3), suggesting that the rate of gain decline is constant, we consider the possibility that the rate of decline may be accelerating, and test for it by fitting more complicated functions to the PHA data.

Though the added radiation exposure is not expected to damage the HRC MCPs, and no obvious change in the rate of gain decline is seen after October 2003 (month 48 in Fig 3), there may be subtle effects detectable at this stage. We search for them by fitting cubic polynomials of the form

$$\text{PHA}(\vec{x}, t) = a(\vec{x}) + b(\vec{x}) \cdot t + c(\vec{x}) \cdot t^2 + d(\vec{x}) \cdot t^3 \quad (1)$$

at each location \vec{x} for time t since October 1999. (As with the linear fits, we exclude the Oct and Dec 99 data at the aimpoint.) Cubics are better suited to detect potentially accelerating regimes of

⁵<http://www.sel.noaa.gov/SolarCycle/>

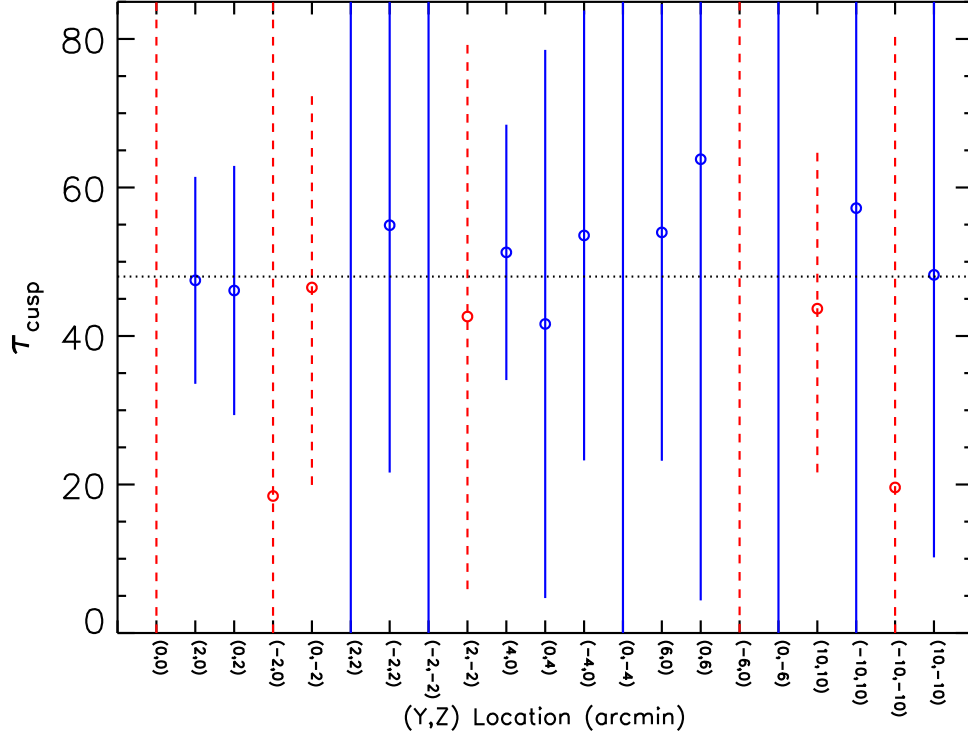


Figure 5: The inflection points of $\text{PHA}(\vec{x},t)$, derived from cubic fits to median PHAs as a function of time. The times at which the rate of decrease in PHA appears to have increased are shown, along with the 1σ errors (vertical lines) for each pointing. The non-physical solutions (see Equation 2) are shown with dashed error bars and the physically meaningful solutions are shown with solid error bars. Note that a majority of the fits, even the physically meaningful ones, have large error bars, indicating that the gain decline does not appear to be accelerating.

decline than linear or quadratic forms; the point where the curvature changes sign,

$$\begin{aligned}
 \frac{d^2\text{PHA}}{dt^2} &\equiv 0 \\
 &= 2c(\vec{x}) + 6d(\vec{x})t, \\
 \text{i.e., } \tau_{\text{cusp}} &= \frac{-c(\vec{x})}{3d(\vec{x})}, \tag{2}
 \end{aligned}$$

generally indicates the time when the decline accelerates. We also compute the statistical error on τ_{cusp} by propagating the errors on the coefficients of the cubic obtained during the fit.

$$\sigma_{\tau} = \frac{-c(\vec{x})}{3d(\vec{x})} \sqrt{\frac{\sigma_{d(\vec{x})}^2}{d(\vec{x})^2} + \frac{\sigma_{c(\vec{x})}^2}{c(\vec{x})^2}} \tag{3}$$

Note that because $\text{PHA}(\vec{x},t)$ always decreases with t , only those solutions that go from concave upwards to concave downwards with increasing t are physically realistic. In this sense, we are imposing such a feature on the $\text{PHA}(\vec{x},t)$ decline and deriving the point at which the decline accelerates. Thus, even if such an event has never occurred, we may still find values of τ_{cusp} in Equation 2 within the applicable range of $0 < t < \sim 80$ months. However, we should not expect to derive a consistent value of τ_{cusp} for all \vec{x} , and furthermore, the error bars on it should be large.

Figure 5 shows these “inflection points” τ_{cusp} for the various observation locations along with the derived 1σ error bars. Note that the majority of the fits result in a physically realistic fit (solid error bars) and a small number result in unphysical solutions (dashed error bars). The unphysical fits invariably have large errors, indicating that they are not well-fit by a cubic, and can thus be ignored. The physically meaningful fits are clustered around the 48-month point, but all of them have large error bars. We therefore conclude that there is no evidence for a rapid decline in gain since October 2003, and the increased dosage expected since then has not affected the HRC-I gain measurably.

5 Time Dependent Gain Correction

In order to calculate time-independent pulse invariant (PI) values, we carry out corrections to $\text{PHA}(\vec{x}, t)$ in two stages. Since the gain decline is linear in time and similar in rate at all monitored locations (see Figure 4), we separate the variables and compute the spatial and temporal gain corrections independently. At each observation epoch, the raw $\text{PHA}(\vec{x}, t)$ are multiplied by a non-linear gain correction surface $g(\vec{x}|t)$ that carries out a “flat-fielding” of the raw PHA values, i.e., at each epoch the PHA at location \vec{x} are transformed to what the PHA are at the aimpoint location. After this “flat-fielding”, the PHA are no longer a function of \vec{x} , and thus will be denoted $\text{PHA}(\vec{0}|t)$. A time dependent correction, $TC(t)$ is then applied to $\text{PHA}(\vec{0}|t)$ to transform them to PI, which are effectively the same as the PI values as on October 1999, when the HRC-I flight voltages were reset. Thus,

$$\begin{aligned} \text{PI} &= \text{PHA}(\vec{x}, t) \times g(\vec{x}|t) \times TC(t) \\ &\equiv \text{PHA}(\vec{0}|t) \times TC(t) \end{aligned} \quad (4)$$

The time-dependent gain correction is currently implemented via a series of gain correction maps, each of which include the effects of both $g(\vec{x}|t)$ and $TC(t)$ for specific epochs. This solution is the least disruptive of existing CALDB and CIAO programs and data structures. Work on producing a more elegant implementation, e.g., via a functional correction, is ongoing.

5.1 Spatial Corrections

We correct for the spatial variations in gain response by creating a series of 7 correction maps $g(\vec{x}|t)$, one from each AO. (We used the Dec 99 dataset when creating the AO1 map.) We compute them as modifications of the high-resolution gain correction map $g_{\text{LAB}}(\vec{x})$ originally derived during ground calibration (Wilton et al. 2005): a corrective factor γ is determined at each pointing, a smooth surface is fit to these corrective factors, and the gain correction map at that epoch is derived as

$$g(\vec{x}|t) = g_{\text{LAB}}(\vec{x}) \times \gamma(\vec{x}|t) \quad (5)$$

This procedure preserves the high spatial-frequency information present in the lab calibration data, while accounting for the gross changes that have occurred in the gain since launch.

The corrective factors γ are computed by a direct comparison of the spectra at different pointings to the aimpoint spectrum. First, the $\text{PHA}(\vec{x}, t)$ are randomized within each bin to avoid aliasing effects, and then the putative spatially gain-corrected PHAs are computed as

$$\text{PHA}_{\text{LAB}}(\vec{x}, t) = \text{PHA}(\vec{x}, t) \cdot g_{\text{LAB}}(\vec{x}). \quad (6)$$

These modified PHAs are binned into spectra $f(\text{PHA})$, and the best-fit value of γ that results in the best match between $f(\gamma \cdot \text{PHA}_{\text{LAB}}(\vec{x}, t))$ and $f(\text{PHA}_{\text{LAB}}(\text{aim}, t))$ is determined via a grid-search

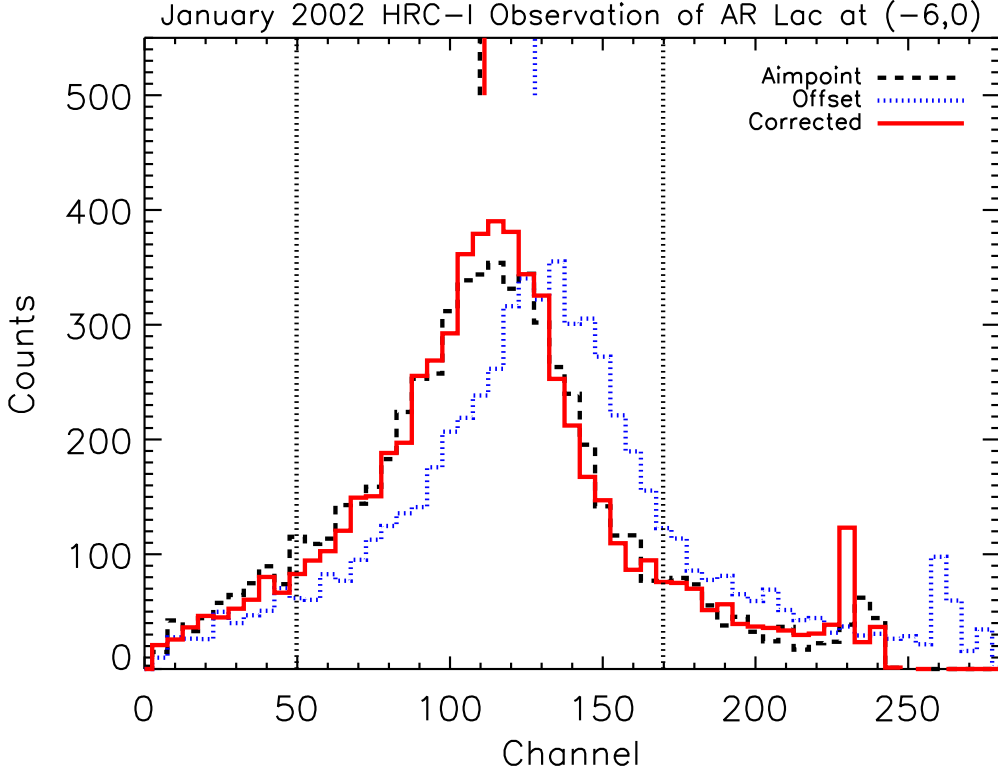


Figure 6: Matching the offset spectrum with the aimpoint spectrum to derive a corrective factor for the gain map. The figure shows the case of the spectrum from the January 2002 AR Lac observation at an offset pointing of $(-6', 0')$ (dotted blue histogram) compared to the aimpoint spectrum (dashed black histogram). The spectra are of the quantities $g_{LAB}(\vec{x}) \cdot PHA(\vec{x}, t)$. A correction factor is determined by imposing a multiplicative corrective factor on the gain until the two spectra match each other (solid red histogram; $PHA_{LAB}(\vec{x}, t)$, $\gamma = 0.875$). The matching is done over PHA values bracketed by the vertical dotted lines. Also shown on the plots as short vertical bars at the top are the locations of the medians of the spectra, in the same style as the corresponding histograms. Note that the off-axis spectra have been normalized to the same number of counts as the aimpoint spectrum.

algorithm ($\gamma = 0.7 : 1.2 : 0.004$) that minimizes the χ^2 value between the two functions. We limited the comparison to values $median(PHA_{LAB}(0, t)) \pm 60$ to minimize the effects of any lingering background counts and outliers. We determine errors by Monte Carlo bootstrapping, generating different realizations of the counts in each bin as Poisson deviations for both spectra 1000 times and recomputing the best-fit in each case. An example of this process is shown in Figure 6.

For each epoch, the corrective factors γ at each of the 21 pointings are calculated⁶ as described above. These correction factors are shown in Figure 7. Next, we use them to interpolate a minimum curvature surface at all locations over the detector to obtain the corrective surface $\gamma(\vec{x}|t)$. This is multiplied by the high-resolution gain map $g_{LAB}(\vec{x})$ to obtain the gain correction map $g(\vec{x}|t)$ for the epoch (Equation 5).

We test the gain correction maps by independently applying $g(\vec{x}|t)$ to the $PHA(\vec{x}, t)$ values and comparing the $median(PHA(\vec{0}|t))$ for all the datasets. The results are shown in Figure 8. As expected, the medians for each epoch are uniform, i.e., the gain correction has removed the spatial

⁶By definition, $\gamma = 1$ at the aimpoint.

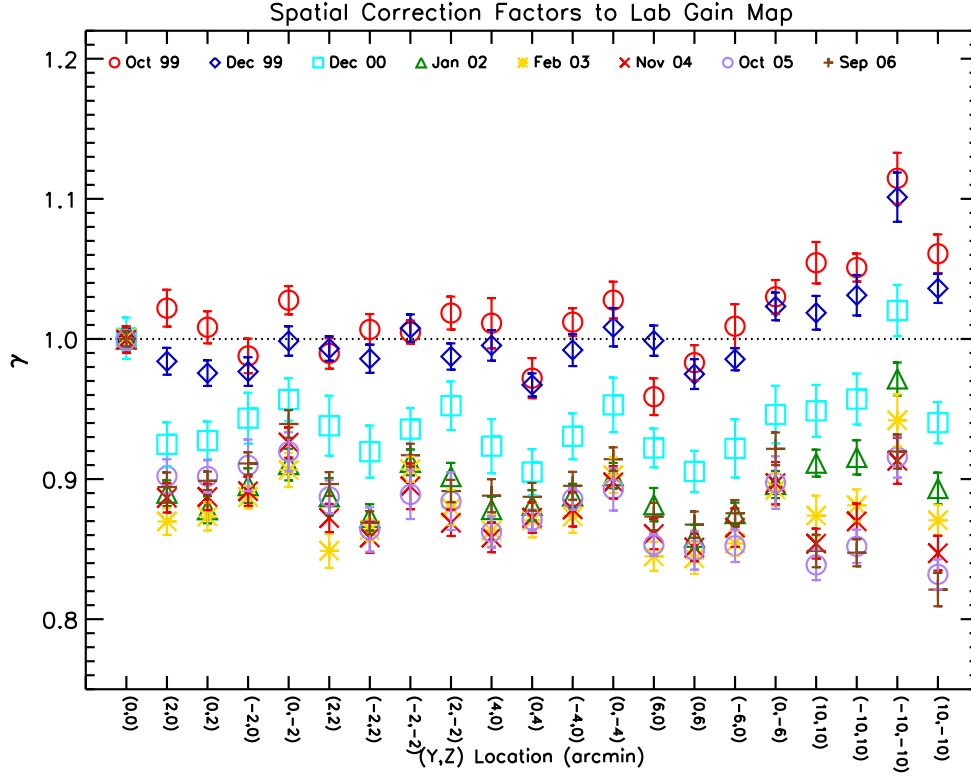


Figure 7: Gain correction factors γ as a function of location on the detector. These correction factors are relative to the pre-flight gain map $g_{\text{LAB}}(\vec{x})$.

dependence in the $\text{PHA}(\vec{x}, t)$. Note that these maps are intermediate products, and are *not* distributed within the calibration database.

5.2 Temporal Correction

Having made correction maps for the spatial non-uniformity of the detector response, our next task is to correct for the time-dependence in the gain decline. As described above, we seek to calculate the correction as a function of time only, and then correct the gain correction maps from each epoch ($g(\vec{x}|t)$, see §5.1) by multiplying with this factor (see Equation 4). That is, we want to find a temporal correction factor (TC) such that

$$PI = \text{PHA}(\vec{0}|t) \times TC(t), \quad (7)$$

where t is the time since October 1999, and PI is the spatially and temporally invariant PHA (that is, matching the flat-field PHA observed at the aimpoint in October 1999), and $\text{PHA}(\vec{0}|t)$ are the flat-field PHA values.

In order to determine $TC(t)$ we proceed as follows. We first fit lines to the medians of the spatially corrected PHA spectra,

$$\text{median}(\text{PHA}(\vec{0}|t)) = m \cdot t + b, \quad (8)$$

for each observation location separately. This results in a set of 21 slopes m and intercepts b . We exclude the October and December 1999 data from all the fits (not just for the aimpoint data) because the sharp non-linear drop in gain between December 1999 and December 2000 (see Figure 3) is now

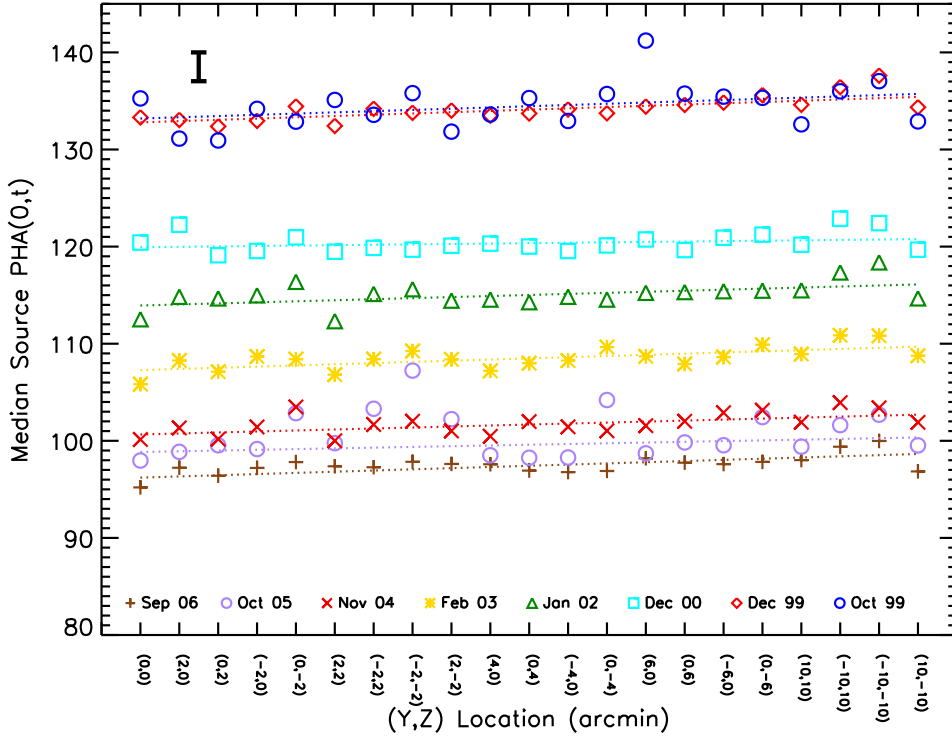


Figure 8: Median “flat-fielded” PHA values as a function of location on the detector, for all the AR Lac observations. The dashed lines show the best-fit line to each set. Since the spatial correction is relative to the aimpoint at each epoch, we expect these lines to be horizontal; the slopes of these lines are statistically indistinguishable from 0. The thick vertical line in the upper left corner shows the typical $\pm 1\sigma$ error on the medians. (Note that this is larger than the error on the raw PHA due to the uncertainty in γ , typically $\sim 1\%$.)

incorporated in $\text{PHA}(\vec{0}|t)$ (compare Figures 2 and 8). The best-fit slopes are shown in Figure 9, and confirm⁷ that the temporal dependence can be modeled as being uniform across the detector, with

$$\bar{m} = \text{mean}(m) = -0.318 \pm 0.014 \text{ channel month}^{-1}. \quad (9)$$

The average y-intercept

$$\bar{b} = \text{mean}(b) = 123.0 \pm 1.6 \text{ channel}, \quad (10)$$

corresponds to the expected value of the median PI during the October 1999 observation if that dataset had followed the linear trend established by the succeeding observations. The observed difference,

$$\Delta \equiv \text{median}(PI|_{\text{Oct99}}) - \bar{b} = 12.29. \quad (11)$$

Including Equations 8 and 11 in Equation 7, we get the form for the time correction for the PHA,

$$TC(t) = \begin{cases} \frac{\bar{b} + \Delta}{\bar{m} \cdot t + \bar{b}} & t > 0 \\ 1 & t = 0 \end{cases} \quad (12)$$

⁷Note that Figure 9 differs from Figure 4 in that the medians of the spatially-corrected PHAs are used rather than the medians of the raw PHAs.

For the gain correction maps from AO2 onwards, the fact that we are implementing the time correction as a step function (with t corresponding to the observation date of the AR Lac set) is not problematic, since the gain change is happening slowly. However, for AO1, when the gain was changing rapidly, a single time correction is not sufficient for the whole time period. This problem is illustrated in §6.1.

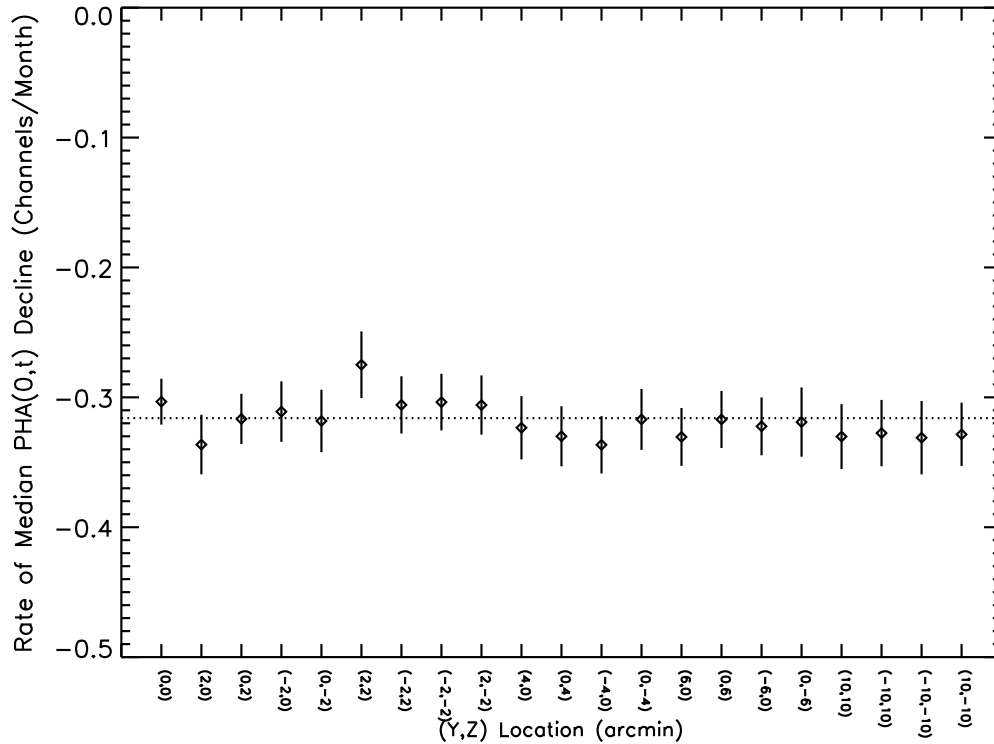


Figure 9: Best-fit slopes (with 1σ errors) from linear fits to the median spatially-corrected PHAs (excluding Oct and Dec 99) for each observation location. The horizontal dashed line shows the average rate of decline.

For each epoch of observation t , we obtain the corresponding correction factor $TC(t)$, and multiply the previously derived “flat-fielded” gain maps $g(\vec{x}|t)$ to obtain the gain correction map at each epoch. These maps, one for each of the 7 epochs, are the final product of our analysis (Figure 10). The first versions of these maps have been available in the calibration database since v3.3. (Updates that are described in detail here, such as including up-to-date reprocessing, accounting for proper background subtraction, accounting for the telemetry saturated times during AO-6, improving the time dependence fits, etc., will be made available in the next CALDB release.)

6 Discussion

6.1 Testing the New Maps

To test the new gain-correction maps, we again return to the raw source and background PHA values extracted from the AR Lac Level 1 event lists (§3). We convert the values to PI using the appropriate map, then find the median background subtracted PI. Figure 11 shows the median PI values for each AO as a function of observation location on the detector. Comparing this figure to raw PHAs versus

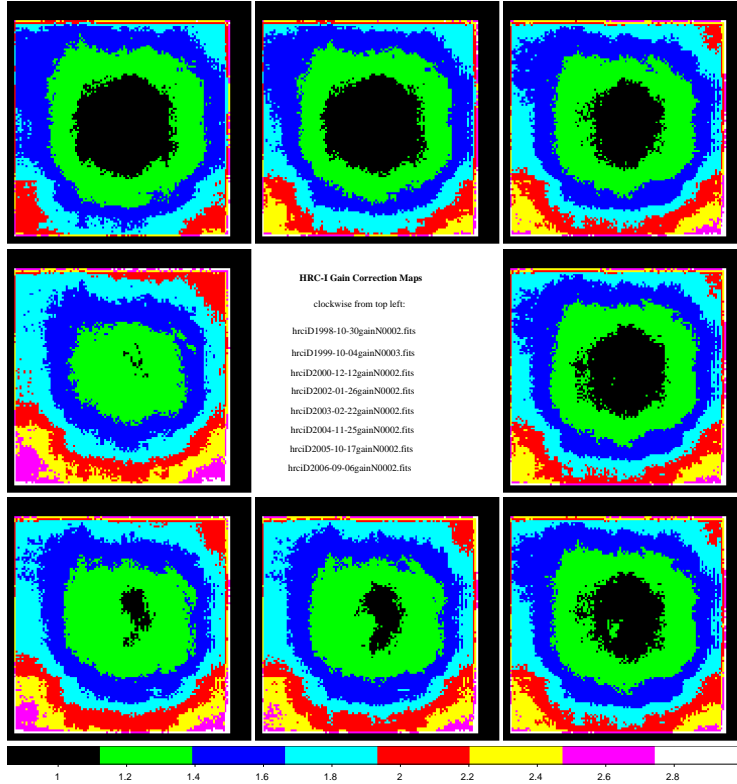


Figure 10: Gain correction maps, shown on a linear display scale from 0.85-3. The pre-flight gain correction map $g_{\text{LAB}}(\vec{x})$ is in the upper left corner. The subsequent time-dependent maps, with updates based on AR Lac observations, are shown chronologically in clockwise order.

location (Figure 2) and spatially-corrected PHAs versus location (Figure 8), we can see that the new gain correction maps have performed their task: the spatial and temporal dependencies from pulse-height values have been removed.

For a more independent test of the newly-created gain correction maps, we use HRC-I calibration observations of the white dwarf HZ 43 (RA = 13:16:21.853, Dec = +29:05:55.44 (FK5)) and the supernova remnant G21.5-0.9 (RA = 18:33:32, Dec = -10:33.6 (FK5)). These sources serve as useful test sets because they have been observed regularly since launch, and therefore we have the opportunity to use each of the time-dependent gain correction maps. In addition, since these sources emit at different energies than AR Lac (peak at ~ 60 eV for HZ 43 and reaching till ~ 2 keV for G21.5, compared to ~ 3 keV for AR Lac), they provide an opportunity to explore the energy dependence (if any) of the gain correction maps. (Unfortunately, we do not have multiple observations of either of these sources at offset locations, so we cannot use them to test the performance of the new gain correction maps away from the aimpoint.)

Figure 12 shows the median source PHAs and PIs as a function of time for HZ 43 and G21.5-09. The gain decline can be seen in the steadily decreasing PHAs over time for both sources. Our new maps successfully remove this effect, as is clear from the linearity over time of the median PIs (calculated by applying the appropriate gain-correction map to the all source PHA values, then finding the median). However, the first three G21.5 points (taken in Oct 99, Feb 00, and Sep 00), and the first HZ 43 point (taken in Feb 00), all converted from PHA with the “AO1” gain correction map, are displaced. This is due to the insufficiency of a constant time-correction over this period

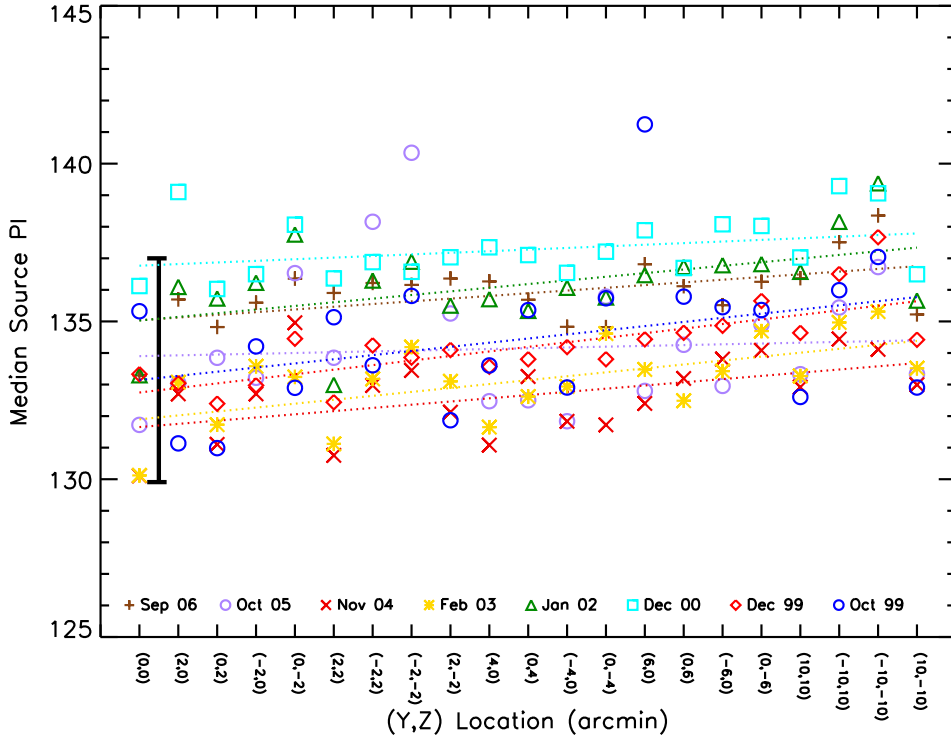


Figure 11: Median PI values of AR Lac datasets, calculated using the new gain correction maps, as a function of observation location. The bold vertical bar at the left shows the typical $\pm 1\sigma$ error on the medians, which includes the uncertainties in γ and $TC(t)$, typically $\sim 1\%$ and $\sim 2\%$, respectively. The horizontal dotted lines show linear least-squares fits to data for each AO. The slopes are statistically consistent with zero.

of time when the gain was changing rapidly. Work is in progress to find a suitable solution to this problem. For now, we warn users to be aware of this issue and to use caution when applying the gain map for data taken between October 1999 and December 2000.

6.2 Correlation with Dosage

Cumulative dosage maps for the HRC-I are made each month by summing the Level 1 event lists from observations taken that month to the previous month's dosage map. Because the dosage is expected to affect the gain, we consider the possibility that the gain decline at a given location on the detector (as evidenced by the median PHA drop at that point between Oct 99 and a later date) is correlated with the cumulative dosage that location received. We explore this relationship in Figure 13. The dosages plotted here are totals from the 800×800 chip x,y regions used when extracting AR Lac events in §3. Surprisingly, we find that there is not a strong correlation between gain decline and dosage. For example, the points at $14.14'$ off-axis and the points at $4'$ off-axis have received roughly the same amount of dosage since launch, 10^6 counts, but the median PHAs in the first group have declined by about 12 channels, while the median PHAs in the second group have declined by ~ 30 channels (see top panel of Figure 13). It seems that areas of the detector where the gain is higher (i.e. near the center) experience relatively larger gain drops than the low gain areas far offaxis. This pattern is seen in the HRC-S as well (Posson-Brown et al., memo in preparation).

However, the dosage maps include only the telemetered events. The total event rate for HRC-I, prior to on-board vetoing, averages to $\sim 250 \text{ cts s}^{-1}$ (Weisskopf et al 2002). This rate is dominated by the particle background which, unlike X-ray events, is not concentrated at the aimpoint. Rather, it is very roughly uniform (to $\pm 20\%$) across the detector (Juda 2002). This may explain why the gain decline does not correspond as strongly to telemetered dosage as we might expect.

Based on lab measurements, we expect a gain decline of 10% after a particle fluence of approximately $6 \times 10^7 \text{ cm}^{-2}$ (Juda 2001), or 6×10^9 events (the detector area is $\sim 100 \text{ cm}^2$). Estimating the average HRC total event rate to be 250 s^{-1} (Weisskopf et al 2002) and the total ONTIME of the detector thus far as $4.4 \times 10^6 \text{ s}$ gives $\sim 1.1 \times 10^9$ counts,⁸ well under the lab limit. Note though that this number is an underestimate, by a factor 2-3x, because the HRC high-voltage (HV) is occasionally on even outside of the observation ONTIME (M.Juda & T.Isobe, private communication). Nevertheless, the fact that we have already seen gain declines $\gg 10\%$ suggests that the correlation of gain decline with dosage may be more complex than expected. We continue to investigate this connection.

7 Summary

By monitoring the background-subtracted median source PHAs from AR Lac observations taken regularly at 21 locations on the HRC-I, we have seen that the detector gain has declined since the beginning of the mission. At the aimpoint, the gain has dropped rapidly between October 1999 and December 2000, with the median PHA falling by 17 channels. Since then, the gain has declined more slowly and linearly, with the median PHA changing at an average rate of ~ -3.7 channels per year at all monitored locations (excluding the four outermost pointings at $14.41'$ off-axis, where the rate is ~ -1.4 channels per year). As of October 2003, the HRC door is kept open at all times; however, we see no evidence of any recent acceleration in the gain drop: leaving the HRC door open has not had a measurable effect on the gain decline.

To address this gain decline, we have made a series of time-dependent gain correction maps by using the AR Lac observations to update the pre-flight gain map. We first derive a set of spatial corrections for each year by comparing the offset to aimpoint AR Lac profiles for that year. We then derive a time correction as a step function of time, based on linear fits to the spatially-corrected PHA values. The final gain correction maps remove the spatial and temporal dependencies from the resulting PI spectra, allowing for direct comparison regardless of observation date or location on the detector. (Note, however, that caution should be used when dealing with observations taken between October 1999 and December 2000.)

Surprisingly, the gain decline is not strongly correlated with the telemetered HRC-I dosage. Even estimating the total HRC-I dosage to date does not explain the magnitude of gain decline seen. We conclude that correlation of the gain decline with dosage is not as expected, and continue to explore this relationship. We also continue to monitor the gain with regular observations of AR Lac, and investigate the possibility of a functional gain correction.

⁸This is larger than the numbers derived from the dosage maps, because the latter includes only events in the Level 1 event lists, whereas the former is the total event rate prior to on-board vetoing.

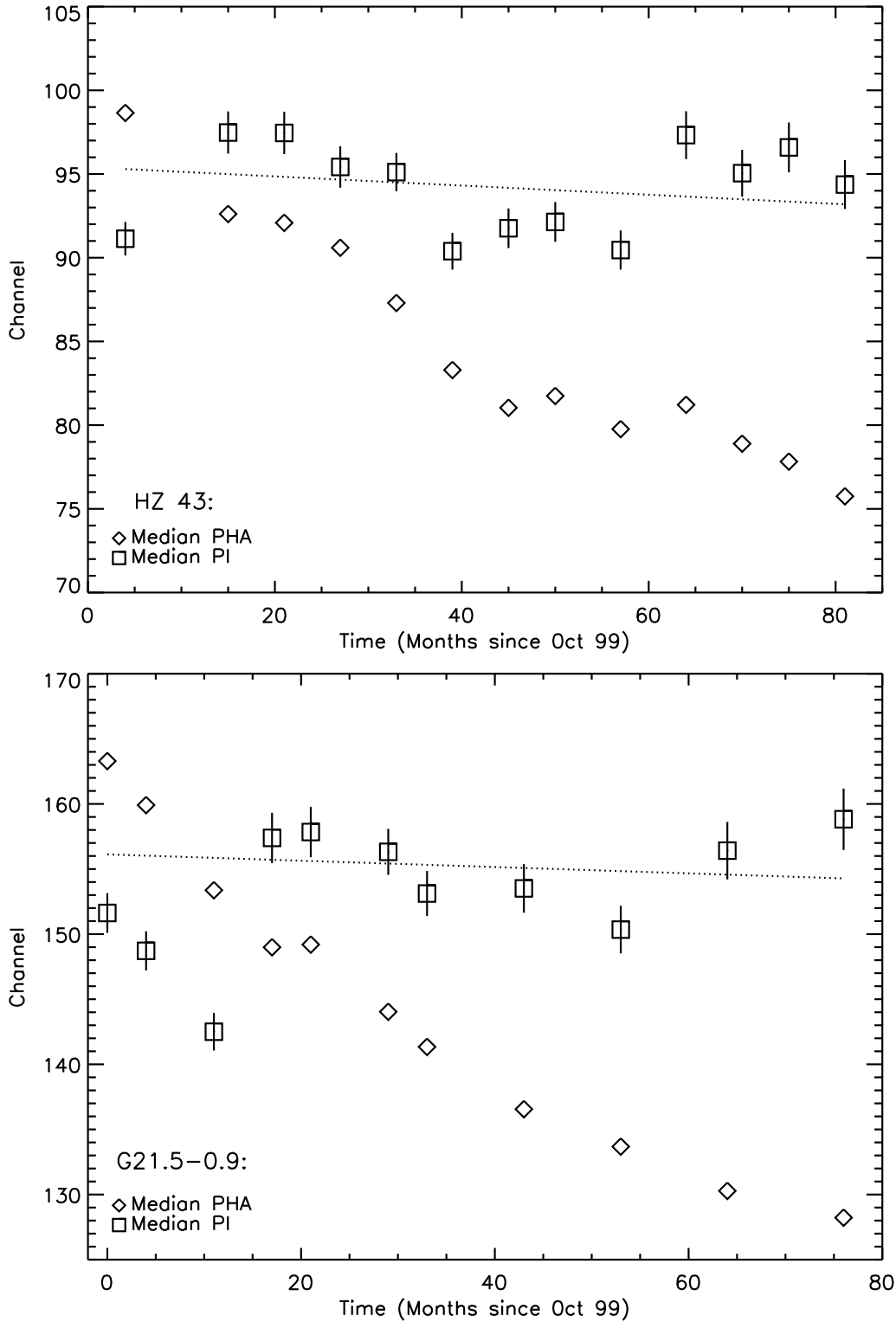


Figure 12: Gain correction for HRC-I calibration observations of HZ 43 (top) and G21.5-0.9 (bottom) for data taken at the detector aimpoint. The diamonds show the median source PHAs, which clearly show the effects of the gain decline. The squares show the median source PIs, calculated using gain correction maps appropriate for the observation date. The dotted lines are linear least-squares fits to the PIs (excluding those calculated with the AO1 map: the first dataset for HZ 43 and the first 3 datasets of G21.5-0.9). The fits are consistent with flatness (slopes of -0.03 ± 0.04 for HZ 43 (top) and -0.02 ± 0.08 for G21.5-0.9 (bottom)), indicating that the gain maps have successfully removed the temporal dependence from the PIs.

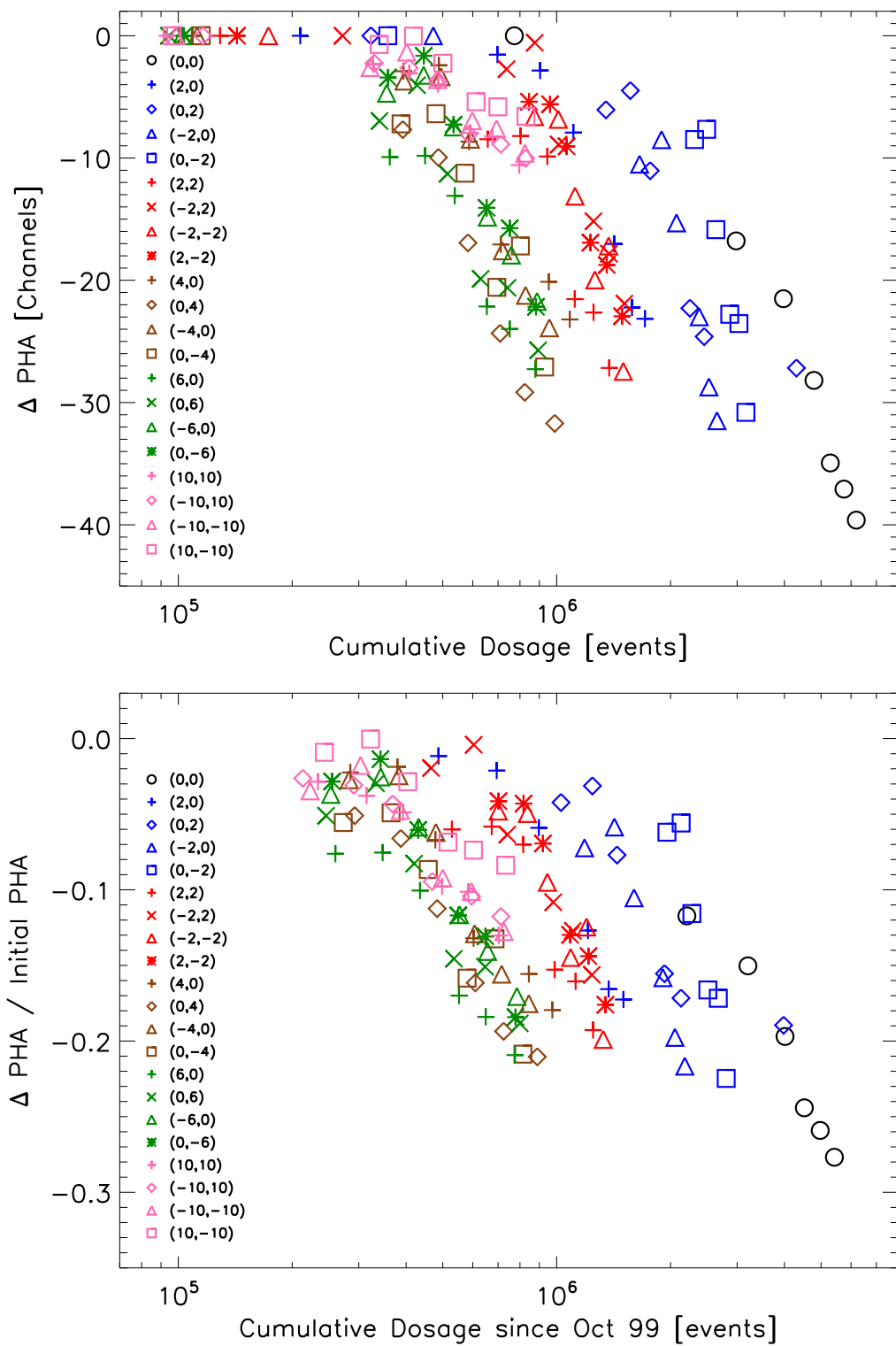


Figure 13: **Top:** The absolute change in median AR Lac PHA as a function of absolute cumulative telemetered dosage since launch. The points at $\Delta \text{PHA} = 0$ show the dosage accumulated at the 21 AR Lac observations locations by October 1999. **Bottom:** The fractional change in median PHA as a function of telemetered dosage accumulated at each location since October 1999. (That is, the dosage received at each location as of October 1999 has been subtracted from the points for that location.) These plots show that the relation between gain decline and dosage is complex and not yet understood.

References

- Juda, M., 2001, *HRC Rates and High Solar Activity* (CXC Memo, available at http://hea-www.harvard.edu/juda/memos/hrc_bkg/high_solar.html)
- Juda, M. et al, 2002, *Proceedings of SPIE*, 4851, 112
- Juda, M., 2004, *HRC-Y Shutter Failure (OCCcm06110): FDB Closeout*, Chandra Flight Note (#441), available at http://hea-www.harvard.edu/juda/memos/shutter_anomaly/shutter_failure.pdf
- Kashyap, V. & Drake, J.J., 2000, *BASI* 28, 475
- Pease, D., Drake, J., 2003, *Monitoring the HRC-S Gain with the LETG/HRC-S* (CXC Memo, available at <http://asc.harvard.edu/cal/Hrc/gain.html>)
- Posson-Brown, J., Donnelly, H., 2003, *Evolution of PHA Response in the HRC*, (CXC Memo, available at <http://asc.harvard.edu/cal/Hrc/gain.html>)
- van Dyk, D.A., Connors, A., Kashyap, V.L., & Siemiginowska, A., 2001, *ApJ*, 548, 224
- Wilton, C., Posson-Brown, J., Juda, M., Kashyap, V., 2005 *The HRC-I Gain Map*, Poster #9.10 at the 2005 Chandra Calibration Workshop, available at http://asc.harvard.edu/ccw/proceedings/05_proc/presentations/wilton/

Table 3: HRC-I AR Lac calibration observations used in creation of the time-dependent gain correction maps.

(Y, Z) Offset [arcmin]	Oct 99			Dec 99			Dec 00			Jan 02		
	ObsID	Exptime [s]	DTCOR									
(0,0)	1321	994.893	0.994	1484	1287.76	0.995	996	3079.97	0.996	2608	1187.59	0.994
(2,0)	1324	994.911	0.995	1485	1279.25	0.994	2345	1182.04	0.988	2617	1186.43	0.994
(0,2)	1342	994.932	0.995	1491	1288.67	0.995	2351	1180.02	0.995	2611	1186.41	0.994
(-2,0)	1336	992.810	0.994	1489	1293.24	0.998	2349	1184.09	0.995	2610	1193.82	0.994
(0,-2)	1330	994.854	0.994	1487	1279.34	0.995	2347	1177.71	0.993	2618	1189.64	0.994
(2,2)	1345	994.893	0.994	1492	1279.76	0.994	2352	1180.02	0.995	2604	1122.47	0.999
(-2,2)	1339	992.794	0.994	1490	1287.82	0.995	2350	1188.19	0.995	2619	1188.50	0.994
(-2,-2)	1333	994.878	0.994	1488	1287.83	0.995	2348	1177.97	0.995	2624	1658.56	0.995
(2,-2)	1327	994.768	0.994	1486	1286.66	0.995	2346	1182.04	0.993	2609	1188.50	0.994
(4,0)	1348	994.927	0.995	1493	1286.80	0.995	2353	1149.96	0.995	2620	1191.83	0.994
(0,4)	1366	994.908	0.995	1499	1286.95	0.995	2359	1189.98	0.995	2606	1197.72	0.994
(-4,0)	1360	994.983	0.995	1497	1286.74	0.995	2357	1189.99	0.995	2621	1186.68	0.994
(0,-4)	1354	994.912	0.995	1495	1288.72	0.995	2355	1177.94	0.995	2612	1193.78	0.994
(6,0)	1351	994.875	0.994	1494	1287.65	0.995	2354	1179.98	0.995	2605	1188.82	0.994
(0,6)	1369	994.901	0.995	1500	1289.40	0.995	2360	1188.90	0.995	2607	1186.77	0.994
(-6,0)	1363	994.946	0.995	1498	1287.84	0.995	2358	1180.00	0.995	2613	1188.64	0.994
(0,-6)	1357	993.032	0.995	1496	1289.85	0.995	2356	1165.67	0.995	2614	1188.62	0.994
(10,10)	1372	994.967	0.995	1501	1288.26	0.995	2361	1189.99	0.995	2615	1186.83	0.995
(-10,10)	1381	8145.72	0.993	1504	1284.88	0.995	2364	1179.96	0.995	2616	1195.73	0.995
(-10,-10)	1378	994.991	0.995	1503	1290.18	0.995	2363	1099.99	0.995	2623	1188.72	0.995
(10,-10)	1375	995.055	0.995	1502	1287.84	0.995	2362	1159.97	0.995	2622	1195.72	0.995
(Y, Z) Offset [arcmin]	Feb 03			Nov 04			Oct 05			Sep 06		
	ObsID	Exptime [s]	DTCOR									
(0,0)	4294	1176.86	0.994	6133	1076.92	0.993	5979	1970.90	0.992	6519	3143.17	0.991
(2,0)	4303	1179.68	0.994	6134	1071.80	0.993	5980	1045.48	0.884	6520	1173.98	0.991
(0,2)	4297	1179.68	0.994	6135	1079.14	0.993	5981	589.796	0.500	6521	1171.12	0.991
(-2,0)	4296	1175.69	0.995	5063	1059.93	0.993	5982	1061.43	0.896	6522	1175.34	0.991
(0,-2)	4304	1177.40	0.994	5064	1068.12	0.993	5983	410.867	0.349	6523	1165.13	0.991
(2,2)	4290	646.692	0.999	5066	1077.09	0.993	5985	539.020	0.457	6525	1169.15	0.991
(-2,2)	4305	1100.07	0.994	5067	1083.02	0.993	5986	383.852	0.323	6526	1172.19	0.991
(-2,-2)	4310	1553.98	0.995	5068	1073.57	0.993	5987	235.416	0.200	6527	1159.18	0.991
(2,-2)	4295	1178.42	0.995	5065	1083.07	0.993	5984	582.467	0.493	6524	1165.45	0.991
(4,0)	4306	1175.64	0.995	5071	1066.16	0.992	5990	1125.68	0.992	6530	1164.40	0.991
(0,4)	4293	1178.96	0.994	5073	1068.13	0.992	5992	1171.31	0.993	6532	1175.32	0.991
(-4,0)	4307	1179.66	0.994	5075	511.306	0.992	5994	1174.03	0.993	6534	1174.22	0.991
(0,-4)	4300	1178.63	0.994	5069	1076.88	0.993	5988	311.304	0.264	6528	1174.21	0.991
(6,0)	4291	886.898	0.991	5072	1066.25	0.992	5991	1166.76	0.993	6531	1171.18	0.991
(0,6)	4292	1175.26	0.994	5074	672.529	0.989	5993	1179.36	0.993	6533	1165.43	0.991
(-6,0)	4299	1182.44	0.994	5076	798.618	0.990	5995	1167.47	0.992	6535	1171.12	0.991
(0,-6)	4298	1173.10	0.994	5070	1077.90	0.993	5989	415.781	0.357	6529	1165.94	0.991
(10,10)	4301	1176.34	0.994	5079	1078.81	0.993	5998	1176.88	0.992	6538	1182.17	0.991
(-10,10)	4302	1173.44	0.994	5080	1073.95	0.993	5999	1164.38	0.992	6539	1174.40	0.991
(-10,-10)	4309	1182.73	0.995	5077	1061.77	0.992	5996	1058.72	0.989	6536	1172.21	0.991
(10,-10)	4308	1173.62	0.995	5078	1078.00	0.993	5997	1148.12	0.990	6537	1164.54	0.991